Heliyon 10 (2024) e26708

Contents lists available at ScienceDirect

Heliyon

journal homepage: www.cell.com/heliyon

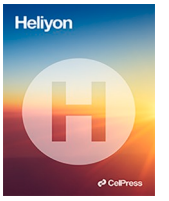

Research article

Structural, morphological, mechanical, and electronic properties of nickel substituted manganese oxide ($Ni_xMn_{1-x}O$, x= 0.0, 0.2, 0.4) for electronic applications

Muhammad Ahmad, Mukhtar Ahmad, Muhammad Hammad Aziz, Muhammad Asif *

Department of Physics, COMSATS University Islamabad, Lahore Campus, 54000, Pakistan

ARTICLE INFO

Keywords:
Manganese oxide
Ni-substitution
Morphology
Mechanical properties
UV-Vis bandgap study

ABSTRACT

The structural, morphological, mechanical, and electronic properties of nickel-substituted manganese oxide ($Ni_xMn_{1-x}O$, where x = 0.0, 0.2, and 0.4) were studied using experimental techniques. The compounds were synthesized using a hydrothermal method. The face-centered cubic structures of the examined compounds were confirmed by XRD. Scanning electron microscopy (SEM) images revealed that the particles were well-shaped, while elemental mapping with energy dispersive spectroscopy (EDS) confirmed that the examined compounds had the appropriate proportions of Ni, Mn, and O. The FT-IR spectroscopy results indicated the respective functional groups. Raman spectroscopy results disclosed the vibration modes of the respective materials. The Tauc plot reveals the semiconducting nature of the compounds. The UV-Vis bandgap study revealed the semiconductor natures of compounds. This demonstrates that these nanoparticles can be used in atom lasers, photovoltaics, and other electronic applications.

1. Introduction

Manganese oxides have been studied a lot over the past 10 years because they could be used in molecular adsorption, ion exchange, catalysis, and energy storage. Manganese oxides that are on the nanometer scale are especially important because their small diameters and large surface areas could lead to different electrical, catalytic, and magnetic properties than those of bulk substances. Several different types of manganese oxide, such as MnO_2, Mn_3O_4, and Mn_2O_3 have been produced. The ferromagnetic nanoclusters of manganese monoxide (MnO) are an intriguing example of an ideal system for the computational investigation of the magnetic and electronic characteristics of oxides [1].

Even though perovskite and rock salt are different in many ways, we think it would be very helpful to look again at the classic electronic structure problem of the "simplest manganese oxide", which is MnO. Manganese oxide is without a doubt one of the chemicals that have been looked at the most in the history of chemistry. Remarkably, despite decades of research, several schools of thought on the electronic structure of MnO coexist, particularly in the realm of electronic structure theories based on first-principles studies. Several of MnO's defining electronic characteristics might vary considerably depending on the approximation used to account for exchange and correlation effects [2].

* Corresponding author.
E-mail address: drmuhammadasif@cuilahore.edu.pk (M. Asif).

https://doi.org/10.1016/j.heliyon.2024.e26708
Received 20 December 2023; Received in revised form 25 January 2024; Accepted 19 February 2024
Available online 22 February 2024

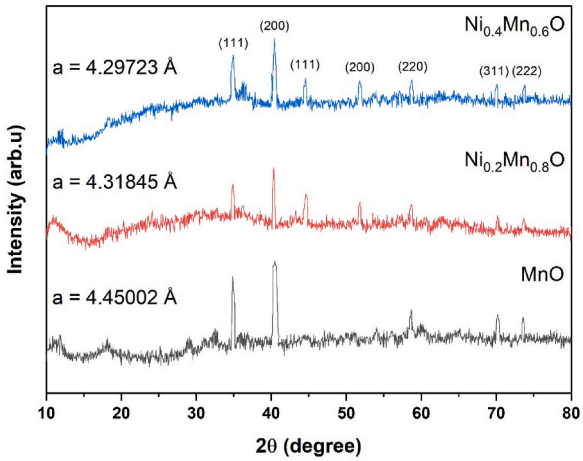

Fig. 1. XRD patterns of (a) MnO, (b) $Ni_{0.2}Mn_{0.8}O$, and (c) $Ni_{0.4}Mn_{0.6}O$

In the past few years, scientists have become very interested in nanostructured materials because they have better chemical and physical properties than their bulk counterparts. When nanomaterials get close to the quantum size domain, they start to show their weird properties. Even so, as the size of systems like nanoparticles, nanowires, and quantum dots decreases, the number of atoms on the material's surface becomes increasingly more dominant than the number of atoms in the bulk's interior, which is charged with special properties of these systems [3].

Nickel is often used to meet specific needs. However, substituting nickel with manganese, which has a smaller atomic radius (r = 135 p.m.) than manganese (r = 140 p.m.) in the crystal lattice, could reduce the bandgap and make the structure less stiff [4]. There are several justifications for asserting that the substitution of nickel will enhance the electrochemical performance [5]. In order to attain these objectives, it is important to conduct an investigation into the impact of nickel substitution on both structure and electronic characteristics [6].

Chemical reduction [7], coprecipitation [8], seeding [7], sono-electrodeposition [7], microwave-assisted method [9], combustion method [10], solvent-deficient method [10], solid-state method [10], inert gas condensation method [9], sputtering [9], laser ablation [9], ultrasound method [9], spark discharge [9], template synthesis [9], biological synthesis [9], sol-gel method [11], solvothermal method [10], hydrothermal method [12,13], microemulsion [12], and inverse microemulsion [7] are all ways to make nanoparticles. The hydrothermal method is ecologically friendly, inexpensive, requires moderate temperatures, and is highly appropriate for advanced material processing. Hydrothermal technology has grown as a potent tool in material processing, beginning with bulk single crystals and progressing to fine and ultrafine crystals, and eventually nanocrystals or nanoparticles [14].

In this present work, for the synthesis of transition metal monoxides (MnO, $Ni_{0.2}Mn_{0.8}O$, and $Ni_{0.4}Mn_{0.6}O$), we employed the hydrothermal technique. Experimental research was conducted to study the structural, morphological, mechanical, and electronic characteristics of these compounds.

2. Procedure

2.1. Experimental procedure

The hydrothermal technique was used for the synthesis of transition metal monoxides (MnO, $Ni_{0.2}Mn_{0.8}O$, and $Ni_{0.4}Mn_{0.6}O$). The preparation procedure for MnO (manganosite, syn) started with 50 ml of D.I. water taken in two beakers one by one. And for the preparation of $Ni_{0.2}Mn_{0.8}O$ and $Ni_{0.4}Mn_{0.6}O$, 35 ml of D.I. water was taken in six beakers individually. After that, the weighted amounts of (0, 0.24, and 0.48) g of nickel (II) chloride hexahydrate ($NiCl_2.6H_2O$), (2, 1.6, and 1.2) g of manganese (II) chloride tetrahydrate ($MnCl_2.4H_2O$), and (0.8, 1.25, and 1.29) g of sodium hydroxide (NaOH) were merged with D.I. water in individual beakers with a magnetic stirrer at room temperature for about 30 minutes to make homogeneous solutions. And for the preparation of MnO, we added NaOH dropwise during the constant stirring of the $MnCl_2.4H_2O$ homogeneous solution. And for the preparation of $Ni_{0.2}Mn_{0.8}O$ and $Ni_{0.4}Mn_{0.6}O$, mixed the homogeneous solutions of $NiCl_2.6H_2O$ and $MnCl_2.4H_2O$, respectively, and after that added NaOH dropwise during the constant stirring of homogeneous solutions; these solutions are then washed three times with D.I. water to get rid of sodium chloride. After washing, the solutions were sealed in a Teflon autoclave separately and heated for 5 h at 180°*C* in the electric oven. Hereafter, the Teflon autoclaves were settled down to room temperature. After removing all the moisture, the samples were crushed into a fine powder using a mortar and pestle. The specific powders were then placed on ceramic boats and calcined for 5 h at 400°*C* in a muffle furnace for single-phase formation. After that, the resultant product was again ground into a fine powder to be characterized with different experimental techniques. The underlying crystal structure of the materials was determined using XRD, but no information regarding their chemical composition was provided. The surface morphology of substances was seen and analyzed using SEM spectroscopy. To visualize and quantify the distribution of different elements inside a sample, EDS elemental mapping was utilized.

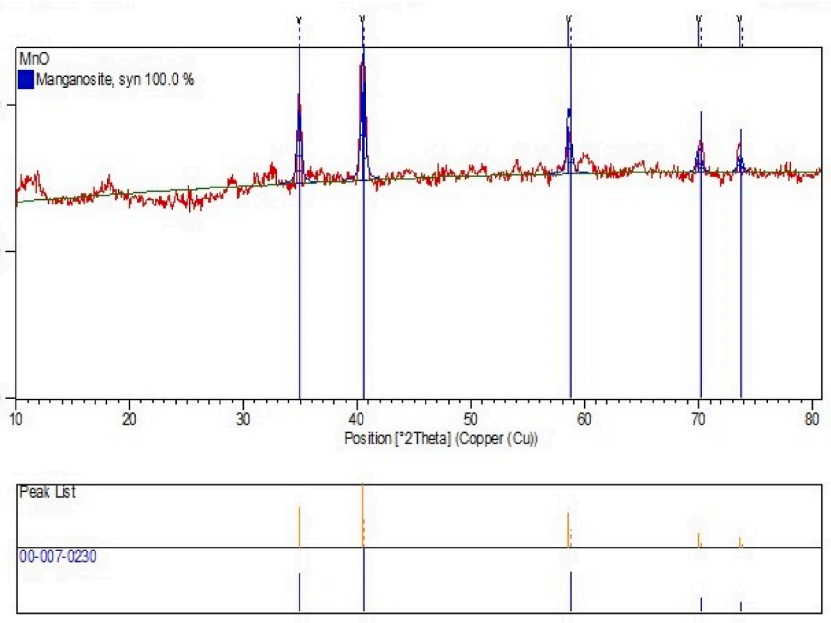

Fig. 2. Rietveld refinement graph of MnO

FTIR spectroscopy provides information on the functional groups and chemical bonds found in materials. Raman spectroscopy was used to investigate the rotational, vibrational, and other low-frequency modes of materials. The bandgap research was analyzed using UV-Vis spectroscopy, which revealed information about its electronic characteristics.

3. Results and discussion

3.1. XRD investigation

The structural depiction of the developed transition metal monoxides (MnO, $Ni_{0.2}Mn_{0.8}O$, and $Ni_{0.4}Mn_{0.6}O$) was done by using Cu-K_α ray having a wave-length of 1.540593 Å, in the span of $(10 \text{ to } 80)^\circ$ for 2θ degrees, as shown in Fig. 1. All of the reflection planes show that the compounds have face-centered cubic structures. Experimental results for pure MnO (manganosite, syn) have been verified by performing Rietveld refinement. The XRD patterns of MnO fitted with powder diffraction file (PDF) No. 00-007-0230 [15] are shown in Fig. 2 and PDF No. 01-089-4835 confirm the existence of MnO peaks at $(44.61^\circ, \text{and } 51.81^\circ)$, and $(44.55^\circ, \text{and } 51.76^\circ)$ 2θ degrees in $Ni_{0.2}Mn_{0.8}O$, and $Ni_{0.4}Mn_{0.6}O$ respectively which are mentioned in the standard of ICDD using X'Pert High-Score Plus program, which means Ni is incorporated very well in MnO. XRD patterns have no additional peaks. It indicates that the materials have a single phase and samples are free of impurities. When the Ni concentration rises, the peaks move upward in angle because the d-spacing changes as metal ions (Ni) are substituted. We investigated the different structural features and the effects of Ni substitution, which we'll talk about below. The lattice constant (a) between the crystal lattice planes was found with the help of the Unit Cell software. The formulas used for calculations of different structural parameters are given below.

The following equation was used to compute the theoretical lattice constant [16];

$$a_{theo} = \frac{8}{3\sqrt{3}}\left[(r_A + R_o) + \sqrt{3}\,(r_B + R_o)\right] \tag{1}$$

The theoretical and experimental results were quite similar.

The crystallite size was calculated using the Debye-Scherrer formula [17,18].

$$D = \frac{K\lambda}{\beta \cos\theta} \tag{2}$$

where D is the size of the crystallite, The Scherrer constant (particle form factor) is K, and its value is 0.9. λ is the radiation wavelength whose value is 1.540593 Å, β is the most intense peak's full-width half maximum (FWHM) (200), and θ is the intense peak's Bragg's angle [19].

By putting the relation [20] on the lattice parameter, the unit cell's volume was found.

$$V = a^3 \tag{3}$$

Table 1
Variation of structural parameters with increasing Ni contents in MnO where ($Ni_xMn_{1-x}O, x = 0.0, 0.2,$ and 0.4)

x	a_{exp} (Å)	a_{theo} (Å)	D (nm)	V $(Å^3)$	D_x (gcm^{-3})
0.0	4.45002	4.45002	20	88.1223	5.3469
0.2	4.31845	4.31845	16	80.5348	5.9126
0.4	4.29723	4.29723	14	79.3534	6.0635

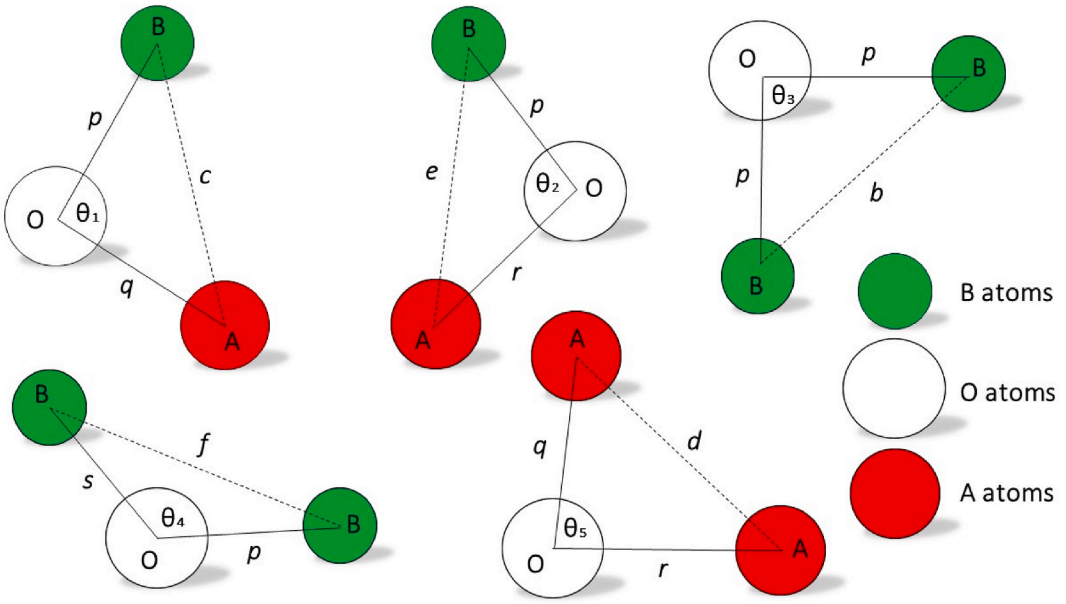

Fig. 3. A graphical illustration of inter-ionic distances and bond angles.

This relationship was used to compute the density of the X-rays [21].

$$D_x = \frac{nM}{N_A V} \tag{4}$$

here, the effective atom number in a unit cell is n; for FCC structure of oxides, the ″n″ value is 4, M denotes the nanoparticles' molar mass, N_A is Avogadro's number with a value of $6.022 \times 10^{23} mol^{-1}$, and the unit cell's volume is V.

Table 1 shows the computed values for all of the parameters stated above. The lattice parameter (a) reduces from 4.45002 Å to 4.29723 Å with Ni-substitution. The disparity in ionic radii between Ni and Mn causes a reduction in the lattice constant. There exists a one-to-one relationship between crystallite size and the lattice parameter. The smaller size of Ni ions causes crystallite size to reduce with increasing Ni substitution. The lattice parameter determines the unit cell's size. The density of X-rays increases as nickel substitution increases.

3.1.1. Inter-ionic distances and bond angles

The cation-cation (Me-Me) distances (b, c, d, e, f) and cation-anion (Me-O) distances (p, q, r, s) are illustrated in Fig. 3 and are determined using established formulae [22,23].

$$p = a\left(\frac{5}{8} - u\right) \tag{5}$$

$$q = a\sqrt{3}\left(u - \frac{1}{4}\right) \tag{6}$$

$$r = a\sqrt{11}\left(u - \frac{1}{4}\right) \tag{7}$$

$$s = \frac{a}{\sqrt{3}}\left(u + \frac{3}{8}\right) \tag{8}$$

Table 2
Inter-ionic distances (p, q, r, s, b, c, d, e, f) values for $Ni_xMn_{1-x}O$ (x = 0.0, 0.2, and 0.4).

x	p (Å)	q (Å)	r (Å)	s (Å)	b (Å)	c (Å)	d (Å)	e (Å)	f (Å)
0.0	1.0858	1.0097	1.9334	1.9423	1.5733	1.8448	1.9269	2.8903	2.7250
0.2	1.0537	0.9798	1.8762	1.8849	1.5268	1.7903	1.8699	2.8049	2.6444
0.4	1.0485	0.9750	1.8670	1.8756	1.5193	1.7815	1.8607	2.7911	2.6315

Table 3
Inter-ionic bond angles $(\theta_1, \theta_2, \theta_3, \theta_4, \theta_5)$ values for $Ni_xMn_{1-x}O$ (x = 0.0, 0.2, and 0.4).

x	θ_1	θ_2	θ_3	θ_4	θ_5
0.0	123.3400	144.9468	92.8536	125.9180	74.4807
0.2	123.3400	144.9468	92.8536	125.9180	74.4807
0.4	123.3400	144.9468	92.8536	125.9180	74.4807

$$b = \frac{\sqrt{2}}{4}a \tag{9}$$

$$c = \frac{\sqrt{11}}{8}a \tag{10}$$

$$d = \frac{\sqrt{3}}{4}a \tag{11}$$

$$e = \frac{3\sqrt{3}}{8}a \tag{12}$$

$$f = \frac{\sqrt{6}}{4}a \tag{13}$$

Because of differences in the lattice constant, cation-anion and cation-cation distances decrease with increasing Ni substitutions. Table 2 shows the computed values for all of these parameters.

The following relationships are used to calculate the inter-ionic bond angles [24,25]:

$$\theta_1 = \cos^{-1}\left(\frac{p^2 + q^2 - c^2}{2pq}\right) \tag{14}$$

$$\theta_2 = \cos^{-1}\left(\frac{p^2 + r^2 - e^2}{2\,pr}\right) \tag{15}$$

$$\theta_3 = \cos^{-1}\left(\frac{2p^2 - b^2}{2p^2}\right) \tag{16}$$

$$\theta_4 = \cos^{-1}\left(\frac{p^2 + s^2 - f^2}{2ps}\right) \tag{17}$$

$$\theta_5 = \cos^{-1}\left(\frac{r^2 + q^2 - d^2}{2rq}\right) \tag{18}$$

There is no change in inter-ionic bond angles after the substitution of Ni, which demonstrates that structures stay unchanged after the substitution. Table 3 shows the computed values for all of these inter-ionic bond angles.

3.1.2. Tetrahedral and octahedral structural parameters

Other parameters at A and B sites were determined using these relationships [26,27], including ionic radii (r_A & r_B), inter-ionic and cationic-anionic distances (R_A & R_B), bond length (d_{AL} & d_{BL}), hopping length (L_A & L_B), shared edge length (d_{ALE} & d_{BLE}), and unshared edge length (d_{BLEU}).

$$r_A = \left(u - \frac{1}{4}\right)a\sqrt{3} - R_o \tag{19}$$

Table 4
Tetrahedral and octahedral site values for $Ni_xMn_{1-x}O$ (x = 0.0, 0.2, and 0.4).

x	r_A (Å)	r_B (Å)	R_A (Å)	R_B (Å)	L_A (Å)	L_B (Å)	d_{AL} (Å)	d_{BL} (Å)	d_{ALE} (Å)	d_{BLE} (Å)	d_{BLEU} (Å)
0.0	−0.3902	−0.3141	1.0097	1.0864	1.9269	1.5733	2.7897	1.0864	1.6488	1.4978	1.5742
0.2	−0.4201	−0.3462	0.9798	1.0543	1.8699	1.5268	2.7072	1.0543	1.6000	1.4535	1.5276
0.4	−0.4249	−0.3514	0.9750	1.0491	1.8607	1.5193	2.6939	1.0491	1.5922	1.4463	1.5201

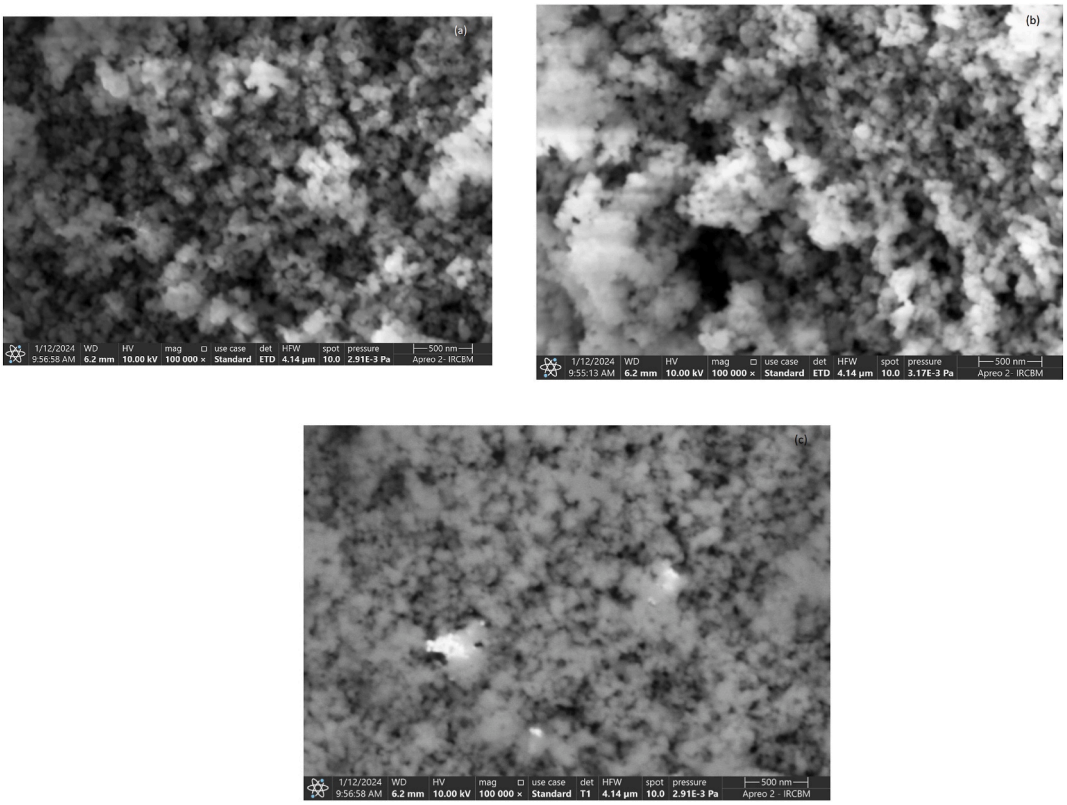

Fig. 4. (a–c): SEM images of (a) MnO, (b) $Ni_{0.2}Mn_{0.8}O$, and (c) $Ni_{0.4}Mn_{0.6}O$.

$$r_B = \left(\frac{5}{8} - u\right)a - R_o \tag{20}$$

$$R_A = a\sqrt{3}\left(\delta + \frac{1}{8}\right) \tag{21}$$

$$R_B = a\sqrt{\left(\frac{1}{16} - \frac{\delta}{2} + 3\delta^2\right)} \tag{22}$$

$$L_A = \frac{1}{4}a\sqrt{3} \tag{23}$$

$$L_B = \frac{1}{4}a\sqrt{2} \tag{24}$$

$$d_{AL} = a\sqrt{3(u - 0.25)} \tag{25}$$

$$d_{BL} = a\left(\sqrt{3u^2 - \frac{11}{4}u + \frac{43}{64}}\right) \tag{26}$$

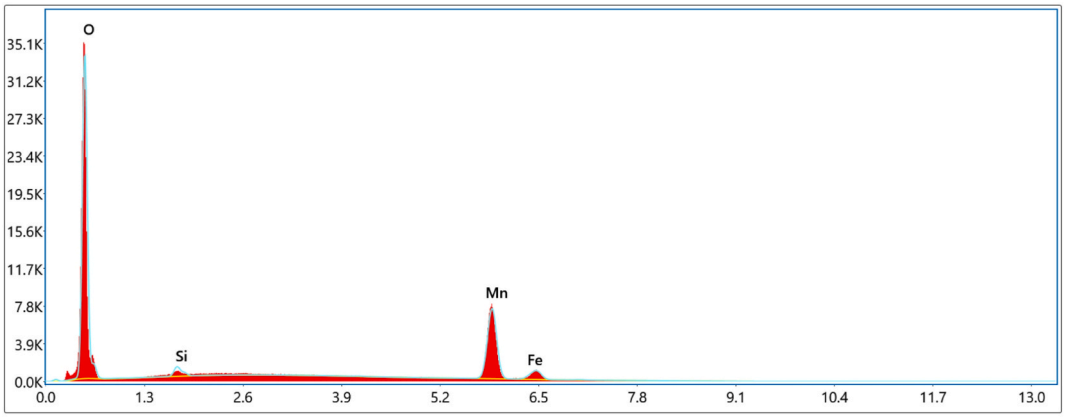

(a) EDX spectrum of MnO.

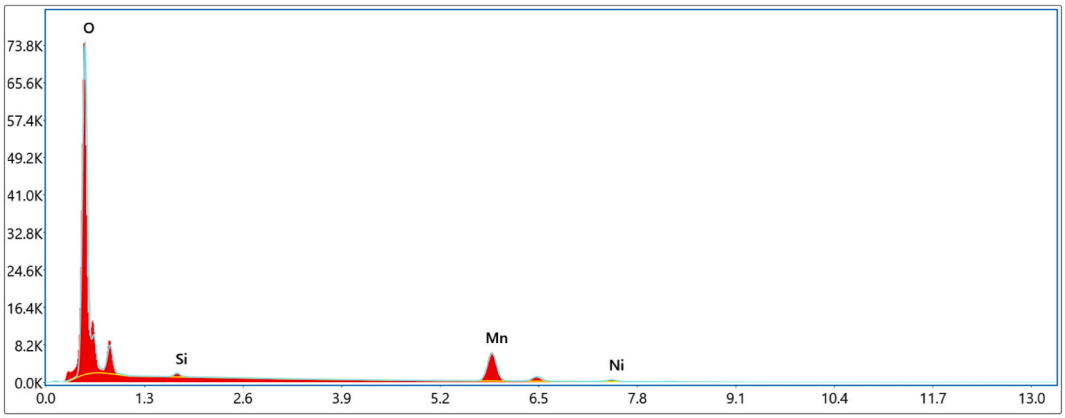

(b) EDX spectrum of $Ni_{0.2}Mn_{0.8}O$.

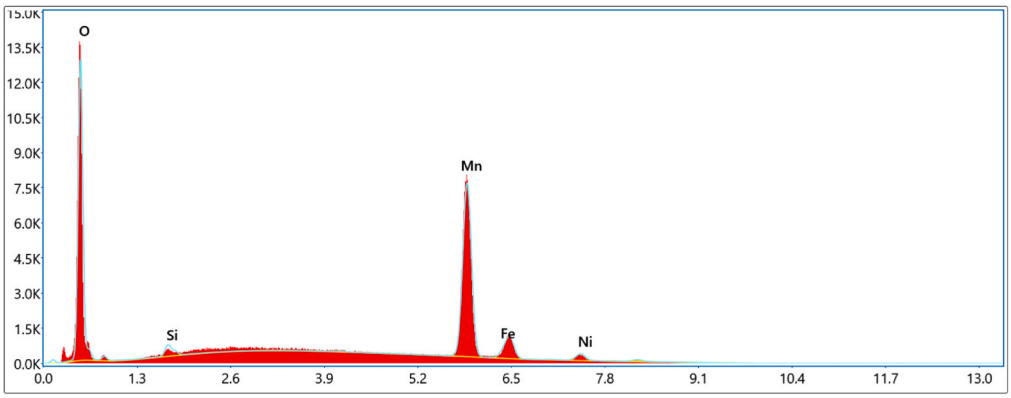

(c) EDX spectrum of $Ni_{0.4}Mn_{0.6}O$.

Fig. 5. (i): EDX spectrum of MnO. (ii): EDX spectrum of $Ni_{0.2}Mn_{0.8}O$. (iii): EDX spectrum of $Ni_{0.4}Mn_{0.6}O$.

Table 5
Quantitative data as determined from EDX analysis for $Ni_xMn_{1-x}O$ (x = 0.0, 0.2, and 0.4).

x = 0.0				x = 0.2				x = 0.4			
Element	Weight%	Atomic%	Error%	Element	Weight%	Atomic%	Error%	Element	Weight%	Atomic%	Error%
O K	56.49	81.09	4.48	O K	71.71	89.32	3.47	O K	35.61	65.13	5.54
SiK	1.84	1.51	7.63	SiK	1.04	0.73	10.03	SiK	1.41	1.47	9.07
MnK	39.68	16.59	1.93	MnK	22.77	8.13	2.17	MnK	57.24	30.49	1.85
FeK	1.98	0.82	11.23	FeK	1.98	0.82	11.23	FeK	2.1	1.1	11.11
NiK	0.00	0.00	0.00	NiK	2.48	0.83	5.98	NiK	3.63	1.81	7.16

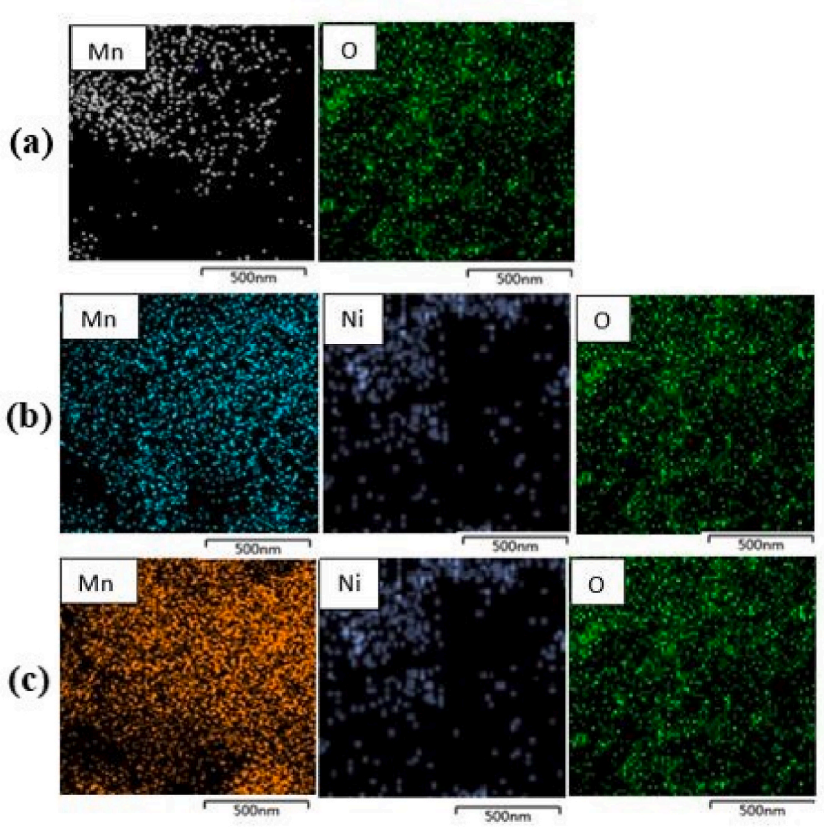

Fig. 6. (a–c): Images of EDS elemental mapping of (a) MnO, (b) $Ni_{0.2}Mn_{0.8}O$, and (c) $Ni_{0.4}Mn_{0.6}O$

$$d_{ALE} = a\sqrt{2}\left(2u - \frac{1}{2}\right) \tag{27}$$

$$d_{BLE} = a\sqrt{2}(1 - 2u) \tag{28}$$

$$d_{BLEU} = a\left(\sqrt{4u^2 - 3u + \frac{11}{16}}\right) \tag{29}$$

where $R_o = 1.40$ Å [28] is the oxygen ion's radius for metal oxides and u = 0.381 is its standard positional parameter. When it comes to FCC structure, $u_{ideal} = 0.375$ is regarded as optimal, and the oxygen parameter's deviation is computed by this relationship: $\delta = u - u_{ideal}$. Table 4 shows the computed values for all of these parameters. The FCC structure is made up of octahedral B and tetrahedral A sites. Mn is found in octahedral locations. Ni is also a promising candidate for octahedral locations. Ni, which has lower radii than Mn, replaces more Mn ions as substitution increases. Because Ni has a lower radius than Mn, all of the parameters reduce as the Ni concentration increases [29].

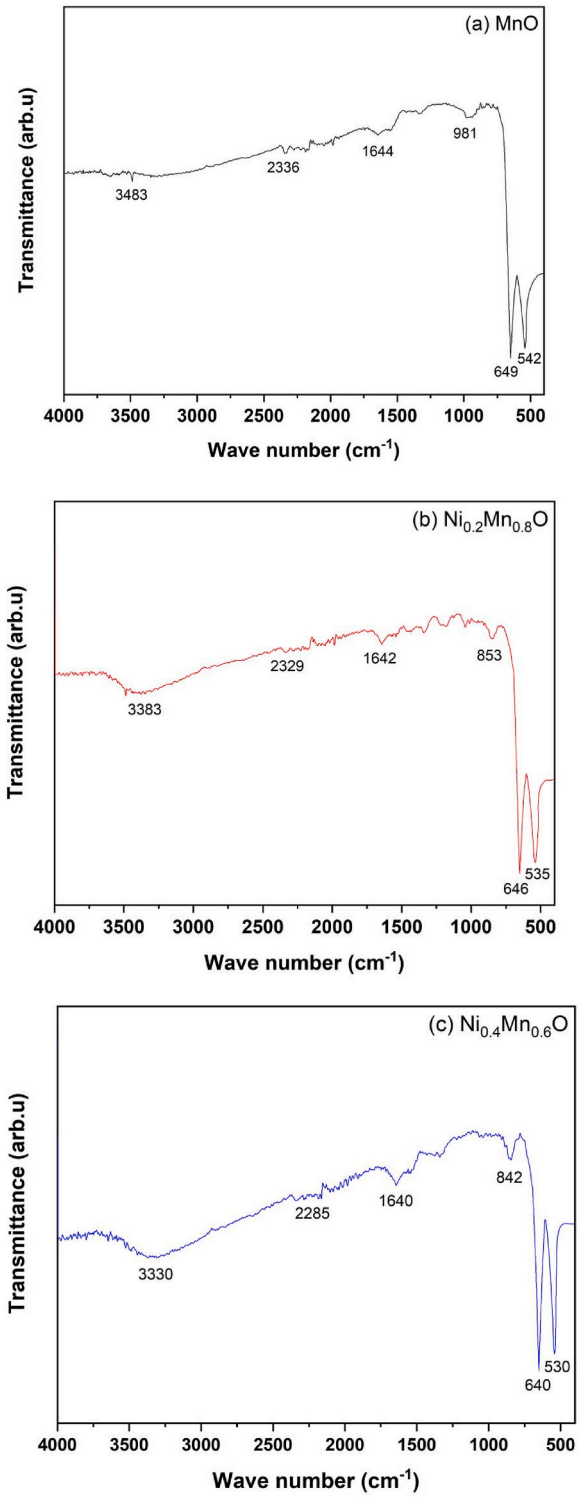

Fig. 7. (a–c): FT-IR spectrum of (a) MnO, (b) $Ni_{0.2}Mn_{0.8}O$, and (c) $Ni_{0.4}Mn_{0.6}O$

3.2. SEM and EDS elemental mapping image examination

The surface morphology of the produced nanoparticles was examined using scanning electron microscopy (SEM). Synthesized nanoparticle MnO, $Ni_{0.2}Mn_{0.8}O$, and $Ni_{0.4}Mn_{0.6}O$ images are in Fig. 4(a–c). The SEM images displayed well-shaped particles, and

several smaller particles were seen. In the MnO image, it was easy to see that the grains were scattered and smaller and that the particles had a trefoil shape with high crystallinity. As Ni is substituted into MnO, differently shaped particles are formed instead of trefoil-shaped particles. The greater precipitation rate during the synthesis process may cause some of the agglomeration that is also seen. According to the line intercept method [30,31], the average grain size of manganese monoxide decreases as the nickel concentration increases, with MnO, $Ni_{0.2}Mn_{0.8}O$, and $Ni_{0.4}Mn_{0.6}O$ having grain sizes of 63 nm, 47 nm, and 35 nm, respectively.

The EDX spectra for some selected samples with MnO, $Ni_{0.2}Mn_{0.8}O$, and $Ni_{0.4}Mn_{0.6}O$ have been shown in Fig. 5(i-iii). The spectra enlighten the presence of Mn, Ni, Fe, Si, and O as the dissolved reactants in the materials without showing any unwanted element as impurity phase. Fe and Si appear in the EDX spectra in all samples because of the sample holder which is made of stainless steel for sample measurements. The observed quantitative data for some representative samples (x = 0.0, 0.2, 0.4) have been provided in Table 5.

The individual elemental mapping images of prepared compounds are shown in Fig. 6(a–c). The atomic weight percentages of the nanoparticles by element are in decent accord with the computed values. SEM-EDS analysis was used to observe the distribution of elements in the nanoparticles. The homogenous distribution of O, Mn, and Ni is observed in the mapped area. All the prepared nanoparticles have uniform incorporation of Mn, EDS elemental mapping confirmed the stoichiometry of the elements in MnO, $Ni_{0.2}Mn_{0.8}O$, and $Ni_{0.4}Mn_{0.6}O$ nanoparticles [32–34].

3.3. FT-IR analysis

Infrared spectroscopy graphs of transition metal monoxide powder are shown in Fig. 7(a–c). The transmittance characteristics of the metal oxide powder have been detected in the scale of 400–4000 cm^{-1}. The chemical bonding of metallic ions and oxide components may be seen via Fourier transform infrared spectroscopy. The MnO, $Ni_{0.2}Mn_{0.8}O$, and $Ni_{0.4}Mn_{0.6}O$ nanoparticles graph shows the absorption peaks at (542, 535, and 530) cm^{-1} and (649, 646, and 640) cm^{-1} arising from the stretching vibrations of the (Mn-*O*-Mn, Ni-*O*-Mn, and Ni-*O*-Mn) and (Mn-O, NiMn-O, and NiMn-O) bonds, which tell us about the octahedral vibration and the tetrahedral vibration, respectively [35]. In addition, strong absorptions at (3483, 3383, and 3330) cm^{-1} and weak absorptions at (2300–3400, 2329, and 2285) cm^{-1} disclose the stretching vibrations of O-H and C-H, respectively. The absorption peaks at (981, 853, and 842) cm^{-1} correspond to the C-OH stretching and OH bending vibrations, respectively, although the bands at (1644, 1642, and 1640) cm^{-1} conform to the C-O (ester, hydroxyl, or ether) stretching and O-H bending vibrations, respectively [36,37]. These findings imply the presence of organic residues on the surface of the as-prepared nanoparticles, such as hydroxyl and carboxyl groups, that are present in the samples due to moisture and combustion of the samples during synthesis.

The IR spectrum of metal oxides tells us a lot about the elastic properties and molecular structure of the material. The Debye temperature is a significant quantity that links the properties of elasticity with thermodynamic properties like specific heat and vibrational entropy. For the synthesized transition metal monoxides, we have determined their Debye temperatures (θ_D) [38] and other parameters by using the following formulas:

$$\theta_D = \lambda_c V_{av} \tag{30}$$

here λ_c is 1.438, and V_{av} stands for the average of tetrahedral V_t and octahedral V_o vibrations. The stiffness of a material determines its elastic properties. The stiffness constants (C_{11} and C_{12}) for FCC oxides are almost equal, which is calculated by the following relation [39]:

$$C_{11} \approx C_{12} = \frac{K}{a} \tag{31}$$

The Bulk modulus (B), Rigidity modulus (R), Young's modulus (Y), and Poisson's ratio (σ) may all be computed using the formulas [39].

$$B = 0.339(C_{11} + 2C_{12}) \tag{32}$$

$$R = D_x V_s^2 \tag{33}$$

$$Y = \frac{9BR}{3B + R} \tag{34}$$

$$\sigma = \frac{Y}{2R} - 1 \tag{35}$$

K is the net force constant, which can be calculated by [39]

$$K = \frac{K_t + K_o}{2} \tag{36}$$

here K_o and K_t are the octahedral and tetrahedral force constants, respectively, which may be computed using the formulas [40,41]

$$K_t = 4\pi^2 V_t^2 c^2 \mu \tag{37}$$

Table 6
Values of FT-IR parameters $(V_t, V_o, \theta_D, \mu, K_t, K_o, K)$ for $Ni_xMn_{1-x}O$ (x = 0.0, 0.2, and 0.4).

x	V_t (cm^{-1})	V_o (cm^{-1})	θ_D (K)	μ (g) $(\times 10^{-23})$	K_t $(\times 10^5)$ $(dynecm^{-1})$	K_o $(\times 10^5)$ $(dynecm^{-1})$	K $(\times 10^5)$ $(dynecm^{-1})$
0.0	649	542	856	2.0575	3.0749	2.1446	2.6098
0.2	646	535	849	0.9742	1.4425	0.9894	1.2159
0.4	640	530	841	1.2261	1.7819	1.2220	1.5019

Table 7
Values of FT-IR parameters $(C_{11}, C_{12}, V_l, V_s, V_m, U)$ for $Ni_xMn_{1-x}O$ (x = 0.0, 0.2, and 0.4).

x	$C_{11} \approx C_{12}$ $(\times 10^4)$	V_l (ms^{-1})	V_s (ms^{-1})	V_m (ms^{-1})	U $(\times 10^{-6})$ (eV)
0.0	5.8647	104.7297	60.4657	67.1284	−0.9934
0.2	2.8158	69.0099	39.8429	44.2331	−0.4359
0.4	3.4952	75.9229	43.8341	48.6642	−0.5331

Table 8
Values of the elastic constant (B, R, Y) and (σ) for $Ni_xMn_{1-x}O$ (x = 0.0, 0.2, and 0.4).

x	B $(\times 10^4)$ (GPa)	R $(\times 10^4)$ (GPa)	Y $(\times 10^4)$ (GPa)	σ
0.0	5.9644	1.9549	5.2870	0.3522
0.2	2.8636	0.9386	2.5384	0.3522
0.4	3.5546	1.1650	3.1509	0.3522

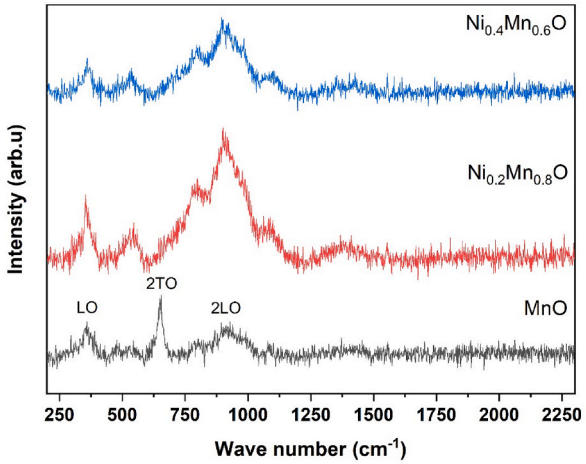

Fig. 8. Raman spectrum of (a) MnO, (b) $Ni_{0.2}Mn_{0.8}O$, and (c) $Ni_{0.4}Mn_{0.6}O$

$$K_o = 4\pi^2 V_o^2 c^2 \mu \tag{38}$$

The speed of light (c) is $2.99792458 \times 10^{10} cms^{-1}$, and the reduced mass (μ) [42] is calculated by

$$\frac{1}{\mu} = \frac{1}{m_1} + \frac{1}{m_2} + \frac{1}{m_3} + \ldots \tag{39}$$

Rearranging the reduced mass formula from the referenced research paper yields the formula for calculating the reduced mass of a compound with three or more elements.here V_s is the transverse velocity and V_l is the longitudinal velocity of the elastic waves, which may be computed using the formulas [42]

$$V_s = \frac{V_l}{\sqrt{3}} \tag{40}$$

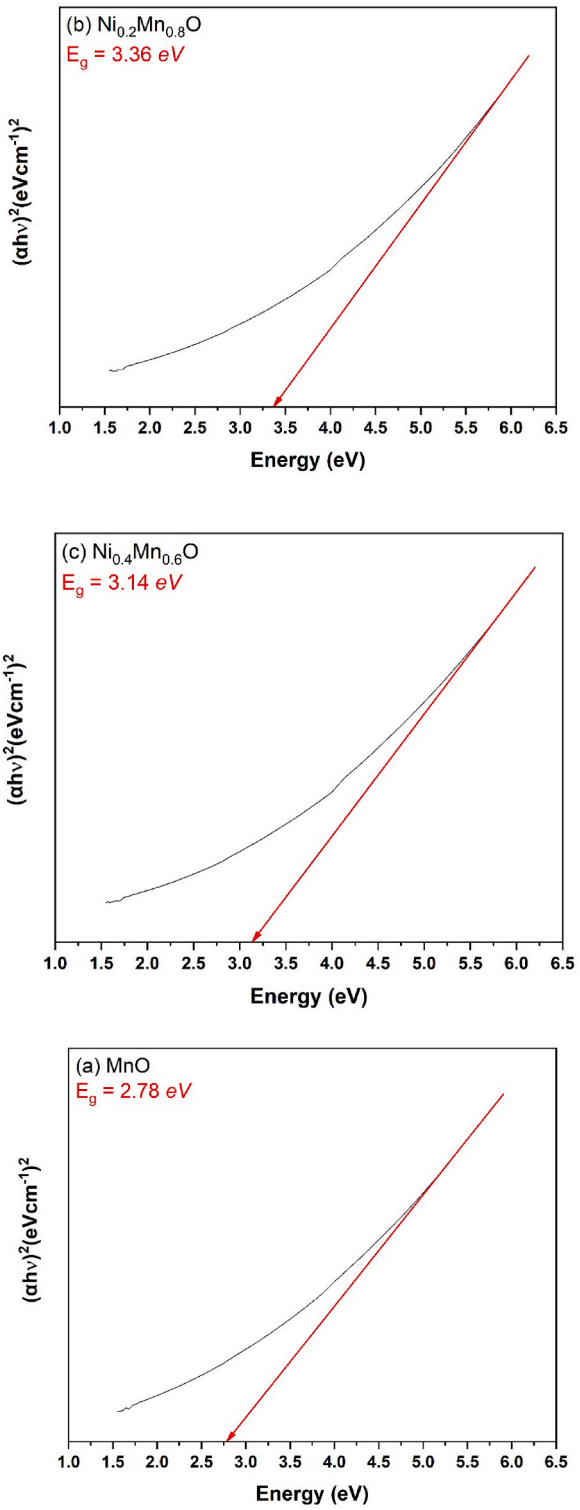

Fig. 9. (a–c): Tauc plot of (a) MnO, (b) $Ni_{0.2}Mn_{0.8}O$, and (c) $Ni_{0.4}Mn_{0.6}O$

$$V_l = \sqrt{\frac{C_{11}}{D_x}} \tag{41}$$

The elastic wave's mean velocity (V_m) [43] and the energy of the lattice *(U)* [39] are computed by

$$V_m = \left[\frac{1}{3}\left(2V_s^{-3} + V_l^{-3}\right)\right]^{-V_3} \tag{42}$$

$$U = -3.108\left(MV_m^2\right) \times 10^{-12} eV \tag{43}$$

When compared to pure MnO, nickel-substituted manganese oxide nanoparticles have different calculated parameter values because their reduced masses are different. Tables 6–8 show the computed values for all of these parameters.

3.4. Raman spectroscopy

Raman spectroscopy is a good way to figure out what transition metal monoxides are made of and how they are put together. Pure manganese oxide has a cubic rock-salt structure at ambient temperature. The Raman spectrum of transition metal monoxides (MnO, $Ni_{0.2}Mn_{0.8}O$, and $Ni_{0.4}Mn_{0.6}O$) shows different frequencies, ranging from (359, 354, and 349) cm^{-1}, (655, 545, and 536) cm^{-1}, and (928, 898, and 895) cm^{-1} which are assigned to longitudinal optical (LO) mode, second-order transverse optical (2TO) mode, and second-order longitudinal optical (2LO) mode, in Fig. 8. Two frequency bands, LO and 2LO, are due to asymmetric vibrations, and the 2TO band is due to symmetric vibration [44]. As nickel is substituted into the manganese oxide, a slight shift of peaks towards lower frequencies is observed. In crystals, atoms vibrate in both longitudinal and transverse directions. For transverse modes, atoms move perpendicular to the wave's path of propagation, while for longitudinal modes, the displacement of atoms from their equilibrium locations corresponds with the direction of the wave.

3.5. UV-Vis band gap study

The optical band gaps E_g for MnO, $Ni_{0.2}Mn_{0.8}O$, and $Ni_{0.4}Mn_{0.6}O$ nanoparticles were computed by the Tauc plot equation [45]:

$$\alpha h\nu = A\left(h\nu - E_g\right)^n \tag{44}$$

Where A is a constant, $h\nu$ is the energy of photon, α is the coefficient of absorption, and factor n is 3/2, 1/2, 2, or 1, which correlate with direct (forbidden), direct (allowed), indirect (forbidden), and indirect (allowed) transitions, respectively. Tauc plots of $(\alpha h\nu)^2$ vs $(h\nu)$ of samples in Fig. 9(a–c) yield the value of the band gap when extrapolated to the baseline [46,47]. The computed band gap values were discovered to be 2.78 *eV* [48], 3.36 *eV*, and 3.14 *eV*, respectively. These results clearly show that as nickel is substituted into manganese oxide, the band gap increases, but there is a decrease in the band gap value of $Ni_{0.4}Mn_{0.6}O$ compared to the $Ni_{0.2}Mn_{0.8}O$ band gap value. These results show the semiconductor nature of materials.

4. Conclusions

The hydrothermal approach was used to successfully produce transition metal monoxide (MnO, $Ni_{0.2}Mn_{0.8}O$, and $Ni_{0.4}Mn_{0.6}O$) nanoparticles. XRD results confirm the cubic shape with faces of all compounds with a lattice constant that varies from 4.45002 to 4.29723 Å. The cation-cation distances, cation-anion distances, and bond angles are calculated by standard formulas and their values vary with the Ni-substitution thereby confirming that all the structural parameters have been altered without the alteration of crystal structure. SEM and EDS elemental mapping images revealed a uniform scattering of Mn, O, and Ni, indicating the formation of well-shaped particles. FT-IR spectra revealed the absorption peak at 530 to 542 cm^{-1} which is due to the octahedral site, and another absorption peak at 640 to 649 cm^{-1} which is due to the tetrahedral site in the metal monoxides. As nickel is substituted into the MnO, these stretching vibrations show a decrease in their values which is since Ni contents have been substituted in the MnO crystal lattice. The Raman spectra of the nanoparticles contain an additional two broad bands. Two frequency bands, LO and 2LO, are due to asymmetric vibrations, and the 2TO band is due to symmetric vibration. As nickel is substituted into the manganese oxide, a slight shift of peaks towards lower frequencies is observed. The bandgap energies calculated by the Tauc equation are found to be 2.78 *eV*, 3.36 *eV*, and 3.14 *eV*, respectively. The UV-Vis bandgap study showed that compounds are semiconductors. This demonstrates that these nanoparticles are suitable for use in atom lasers, photovoltaics, and other electronic applications.

CRediT authorship contribution statement

Muhammad Ahmad: Writing – original draft, Methodology, Investigation, Conceptualization. **Mukhtar Ahmad:** Writing – review & editing, Writing – original draft, Supervision, Methodology, Conceptualization. **Muhammad Hammad Aziz:** Conceptualization, Investigation, Writing – original draft. **Muhammad Asif:** Writing – review & editing, Supervision, Investigation, Formal analysis, Conceptualization.

Declaration of competing interest

The authors declare that they have no known competing financial interests or personal relationships that could have appeared to influence the work reported in this paper.

References

[1] M. Zheng, et al., A simple additive-free approach for the synthesis of uniform manganese monoxide nanorods with large specific surface area, Nanoscale Res. Lett. 8 (2013) 1–7.
[2] I. Solovyev, K. Terakura, Effective single-particle potentials for MnO in light of interatomic magnetic interactions: existing theories and perspectives, Phys. Rev. B 58 (23) (1998) 15496.
[3] D. Romero-Fierro, et al., Polymer-magnetic semiconductor nanocomposites for industrial electronic applications, Polymers 14 (12) (2022) 2467.
[4] R.E. Khalfaouy, et al., Nickel-substituted LiMnPO4/C olivine cathode material: combustion synthesis, characterization and electrochemical performances, Ceram. Int. 45 (14) (2019) 17688–17695.
[5] B. Wang, et al., Gradient substitution: an intrinsic strategy towards high performance sodium storage in Prussian blue-based cathodes, J. Mater. Chem. A 6 (19) (2018) 8947–8954.
[6] M. Ahmed, et al., Effect of Ni substitution on the structural and transport properties of NixMn0. 8− xMg0. 2Fe2O4; 0.0≤ x≤ 0.40 ferrite, J. Alloys Compd. 509 (3) (2011) 805–808.
[7] N.H. Nam, N.H. Luong, Nanoparticles: synthesis and applications, in: Materials for Biomedical Engineering, Elsevier, 2019, pp. 211–240.
[8] J. Chandradass, et al., Influence of processing methodology on the structural and magnetic behavior of MgFe2O4 nanopowders, J. Alloys Compd. 517 (2012) 164–169.
[9] A.V. Rane, et al., Methods for synthesis of nanoparticles and fabrication of nanocomposites, in: Synthesis of Inorganic Nanomaterials, Elsevier, 2018, pp. 121–139.
[10] M.J. Uddin, Y.-K. Jeong, Adsorptive removal of pollutants from water using magnesium ferrite nanoadsorbent: a promising future material for water purification, Environ. Sci. Pollut. Control Ser. (2021) 1–26.
[11] N. Kaur, M. Kaur, Comparative studies on impact of synthesis methods on structural and magnetic properties of magnesium ferrite nanoparticles, Processing and Application of Ceramics 8 (3) (2014) 137–143.
[12] K. Hachem, et al., Methods of chemical synthesis in the synthesis of nanomaterial and nanoparticles by the chemical deposition method: a review, BioNanoScience 12 (3) (2022) 1032–1057.
[13] C. Aoopngan, et al., Amine-functionalized and hydroxyl-functionalized magnesium ferrite nanoparticles for Congo red adsorption, ACS Appl. Nano Mater. 2 (8) (2019) 5329–5341.
[14] M. Yoshimura, K. Byrappa, Hydrothermal processing of materials: past, present and future, J. Mater. Sci. 43 (2008) 2085–2103.
[15] Y. Lin, et al., Petal cell-derived MnO nanoparticle-incorporated biocarbon composite and its enhanced lithium storage performance, J. Mater. Sci. 55 (5) (2020) 2139–2154.
[16] N. Abu-Elsaad, Elastic properties of germanium substituted lithium ferrite, J. Mol. Struct. 1075 (2014) 546–550.
[17] M. Ajmal, et al., The influence of Ga doping on structural magnetic and dielectric properties of NiCr0. 2Fe1. 8O4 spinel ferrite, Phys. B Condens. Matter 526 (2017) 149–154.
[18] M. Sithole, et al., Visible light active gC 3 N 4 sheets/CdS heterojunction photocatalyst for decolourisation of acid blue (AB-25), J. Nanoparticle Res. 23 (2021) 1–17.
[19] M.J. Iqbal, S. Farooq, Effect of doping of divalent and trivalent metal ions on the structural and electrical properties of magnesium aluminate, Mater. Sci. Eng., B 136 (2–3) (2007) 140–147.
[20] A.A. Ati, et al., Structural and magnetic properties of Co–Al substituted Ni ferrites synthesized by co-precipitation method, J. Mol. Struct. 1058 (2014) 136–141.
[21] M. Ahmad, et al., Lithium ferrite (Li0. 5Fe2. 5O4): synthesis, structural, morphological and magnetic evaluation for storage devices, J. Mater. Res. Technol. 18 (2022) 3386–3395.
[22] N. Vasoya, et al., Study on the electrical and dielectric behaviour of Zn-substituted cobalt ferrialuminates, J. Phys. Condens. Matter 18 (34) (2006) 8063.
[23] Z. Yan, J. Luo, Effects of CeZn co-substitution on structure, magnetic and microwave absorption properties of nickel ferrite nanoparticles, J. Alloys Compd. 695 (2017) 1185–1195.
[24] V. Lakhani, et al., Structural parameters and X-ray Debye temperature determination study on copper-ferrite-aluminates, Solid State Sci. 13 (3) (2011) 539–547.
[25] G. Kumar, et al., Superparamagnetic behaviour and evidence of weakening in super-exchange interactions with the substitution of Gd3+ ions in the Mg–Mn nanoferrite matrix, Mater. Res. Bull. 63 (2015) 216–225.
[26] M.Z. Khan, et al., Comprehensive study on structural, electrical, magnetic and photocatalytic degradation properties of Al3+ ions substituted nickel ferrites nanoparticles, J. Alloys Compd. 848 (2020) 155795.
[27] S.B. Somvanshi, et al., Structural, thermal, spectral, optical and surface analysis of rare earth metal ion (Gd3+) doped mixed Zn–Mg nano-spinel ferrites, Ceram. Int. 46 (9) (2020) 13170–13179.
[28] M. Bindhu, et al., Synthesis and characterization of zinc oxide nanostructures and its assessment on enhanced bacterial inhibition and photocatalytic degradation, J. Photochem. Photobiol. B Biol. 210 (2020) 111965.
[29] S. Hassan, et al., Structural, magnetic and electrochemical properties of Al-substituted Ni ferrites for energy storage devices, J. Energy Storage 55 (2022) 105320.
[30] M.N. Akhtar, et al., Structural rietveld refinement, morphological and magnetic features of Cu doped CoCe nanocrystalline ferrites for high frequency applications, Phys. B Condens. Matter 561 (2019) 121–131.
[31] M.N. Akhtar, et al., Evaluation of structural, morphological and magnetic properties of CuZnNi (CuxZn0. 5− xNi0. 5Fe2O4) nanocrystalline ferrites for core, switching and MLCI's applications, J. Magn. Magn Mater. 421 (2017) 260–268.
[32] T.G. Ritter, et al., Electrochemical synthesis of high entropy hydroxides and oxides boosted by hydrogen evolution reaction, Cell Reports Physical Science 3 (4) (2022).
[33] X. He, et al., Enhanced electrochemical performance in lithium ion batteries of a hollow spherical lithium-rich cathode material synthesized by a molten salt method, Nano Res. 7 (2014) 110–118.
[34] H. Sone, et al., Thermal plasma synthesis and electrochemical properties of high-voltage LiNi0. 5Mn1. 5O4 nanoparticles, Mater. Res. Express 7 (1) (2019) 015015.
[35] H. Chen, J. He, Facile synthesis of monodisperse manganese oxide nanostructures and their application in water treatment, J. Phys. Chem. C 112 (45) (2008) 17540–17545.
[36] M. Zheng, et al., Alcohol-assisted hydrothermal carbonization to fabricate spheroidal carbons with a tunable shape and aspect ratio, Carbon 48 (4) (2010) 1224–1233.
[37] M. Sevilla, A.B. Fuertes, Chemical and structural properties of carbonaceous products obtained by hydrothermal carbonization of saccharides, Chem.–Eur. J. 15 (16) (2009) 4195–4203.
[38] S. Patange, et al., Infrared spectral and elastic moduli study of NiFe2− xCrxO4 nanocrystalline ferrites, J. Magn. Magn Mater. 325 (2013) 107–111.
[39] A. ur Rehman, et al., Ba substituted SrFe2O4 (SrBa0. 3Fe1. 7O4) for the removal of fluoride ions (F− 1) from the drinking water, Mater. Chem. Phys. 295 (2023) 127165.

[40] M.N. Akhtar, et al., Structural, magnetic, dielectric and high frequency response of synthesized rare earth doped bismuth nano garnets (BIG), Results Phys. 10 (2018) 784–793.
[41] M.N. Akhtar, et al., Structural and electromagnetic evaluations of YIG rare earth doped (Gd, Pr, Ho, Yb) nanoferrites for high frequency applications, Ceram. Int. 43 (18) (2017) 17032–17040.
[42] S. Mazen, H. Elsayed, N. Abu-Elsaad, A comparative study of different concentrations of (Co/Ni/Cu) effects on elastic properties of Li–Mn ferrite employing IR spectroscopy and ultrasonic measurement, Ceram. Int. 47 (19) (2021) 26635–26642.
[43] A. Anupama, et al., Composition dependent elastic and thermal properties of LiZn ferrites, J. Alloys Compd. 728 (2017) 1091–1100.
[44] N. Mironova-Ulmane, et al., Synthesis and Vibration Spectroscopy of Nano-Sized Manganese Oxides, 2018.
[45] A.J. Kadhm, R.A. Ismail, A.F. Atwan, Fabrication of visible-enhanced nanostructured Mn2O3/Si heterojunction photodetector by rapid thermal oxidation, Silicon 14 (10) (2022) 5297–5310.
[46] D. Dubal, et al., Chemical synthesis and characterization of Mn3O4 thin films for supercapacitor application, J. Alloys Compd. 497 (1–2) (2010) 166–170.
[47] M. Fakharpour, M.H.K. Tafti, The energy band gap of the manganese oxide pyramidal nanostructures, J. Mod. Opt. 69 (16) (2022) 911–916.
[48] M. Touqeer, et al., New Co-MnO based Nanocrsytallite for photocatalysis studies driven by visible light, J. Taibah Univ. Sci. 14 (1) (2020) 1580–1589.